2017

Predicting Steel Tensile Responses and Fracture Using the Phenomenological Ductile Shear Fracture Model

Kazeem K. Adewole
University of Ibadan

Lip H. Teh
University of Wollongong, lteh@uow.edu.au

Predicting Steel Tensile Responses and Fracture Using the Phenomenological Ductile Shear Fracture Model

Abstract

In the literature, all the micromechanical fracture models used for predicting structural steel tensile responses and fracture are based on the ductile fracture mechanism that uses the Lode angle parameter to simulate shear fracture under low-stress triaxiality. Using the phenomenological shear fracture model that uses the shear stress ratio rather than the Lode angle parameter, this technical note presents the finite element predictions of the responses of S690 steel solid and perforated coupons under tension and of the fractures of TRIP (transformation-induced plasticity) 690 steel specimens under pure shear and combined shear and tension. The calibrated phenomenological shear fracture model parameters are obtained through a phenomenological curve-fitting process that does not involve costly laboratory tests. This technical note demonstrates that the phenomenological shear fracture model can accurately predict the responses and fracture of structural steels under tension, pure shear, and combined shear and tension.

Publication Details

Adewole, K. K. & Teh, L. H. (2017). Predicting Steel Tensile Responses and Fracture Using the Phenomenological Ductile Shear Fracture Model. Journal of Materials in Civil Engineering, 29 (12), 06017019-1-06017019-6.

Predicting steel tensile responses and fracture using the phenomenological ductile shear fracture model

Kazeem K. Adewole[1] and Lip H. Teh[2] M.ASCE

ABSTRACT

In the literature, all the micromechanical fracture models employed for predicting structural steel tensile responses and fracture are based on the ductile fracture mechanism which employed the Lode angle parameter to simulate shear fracture under low stress triaxiality. Using the phenomenological shear fracture model that employs the shear stress ratio rather than the Lode angle parameter, this technical note presents the finite element predictions of the responses of S690 steel solid and perforated coupons under tension, and of the fractures of TRIP (Transformation Induced Plasticity) 690 steel specimens under pure shear and under combined shear and tension. The calibrated phenomenological shear fracture model parameters are obtained through phenomenological curve fitting process that does not involve costly laboratory tests. This technical note demonstrates that the phenomenological shear fracture model can accurately predict the responses and fracture of structural steels under tension, pure shear and combined shear and tension.

Keywords: ductile shear fracture, ductile tensile fracture, phenomenological fracture model, steel fracture, void growth mechanism

[1]Lecturer, Civil Engineering Department, University of Ibadan, Ibadan, Nigeria,
E-mail: kkadewole@yahoo.com
[2]Associate Professor, School of Civil, Mining and Environmental Engineering,
Univ. of Wollongong, Wollongong, NSW 2500, Australia E-mail: lteh@uow.edu.au

Introduction

Ductile materials exhibit two types of fracture: “ductile shear fracture” and “ductile tensile fracture” (Björklund and Nilsson 2014). Either mode or a combination of both may take place in structural steel (Hooputra et al. 2004, Björklund et al. 2013). Fracture initiation in the shear mode occurs under intense shear stresses resulting either from extensive slip on the activated slip planes and/or microcracking without any void nucleation, or from void nucleation in the slip bands (French and Weinrich 1979). In any case, the shear mode is less pressure-dependent than the tensile mode (Björklund et al. 2013).

In the tensile mode, fracture initiation is always associated with void nucleation under predominantly tensile stresses at high stress triaxiality (Björklund et al. 2013). The growth and coalescence of nucleated voids in this mode occur under varying stress conditions with varying fracture mechanisms as the ductile fracture propagates (Danas and Castañeda 2014). The initial growth and coalescence, which are associated with inter-void ligaments necking, occur under high stress triaxiality and pure hydrostatic stress. The growth and coalescence then takes place under intermediate and subsequently low stress triaxiality. Under the intermediate stress triaxiality, a transition from the predominantly tensile stresses-based void growth mechanism to the predominantly shear stresses-based void shearing mechanism occurs (Danas and Castañeda 2012).

The Gurson-Tvergaard-Needleman model or Gurson-like models (Cockroft and Latham 1968, Wilkins et al. 1980, Gologanu et al. 1993) and the Rice and Tracey’s void growth model or its variants (Rice and Tracey 1969, Kanvinde & Deierlein 2006, Jia and Kuwamura 2013, Kiran and Khandelwal 2013) have been employed to simulate the void nucleation, growth, and coalescence fracture mechanism. However, these models generally fail to predict predominantly

shear fracture under low and negative stress triaxiality (Danas and Castañe 2012, Wen and Mahmoud 2015). A parameter that improves the simulation in the later stage of the ductile fracture mode under low stress triaxiality, called the Lode angle, has been used to simulate the void shearing effect (Xue 2008, Nahshon and Hutchinson 2008, Bai and Wierzbicki 2008, Danas and Castañe 2012, Cheng et al. 2015, Wen and Mahmoud 2015, Li et al. 2016). The Lode angle is used to distinguish the different shear stress states in three dimensions.

In any case, all the aforementioned models require a number of parameters (up to nine) that are to be calibrated from elaborate laboratory tests, with some requiring fractographic analysis. Costly laboratory tests are therefore required to obtain the calibrated parameters (Bernauer and Brocks 2002), which are not feasible for most design firms (Kiran and Khandelwal 2013).

An economical method for obtaining the required fracture parameters is the phenomenological curve fitting process. The phenomenological curve fitting process involves keeping some parameters constant while varying others during numerical simulations until the simulation results match the experimental results up to the displacement at fracture (Bernauer and Brocks 2002). The parameters at which the simulated displacement at fracture matches the experimental displacement are the set of critical/calibrated fracture parameters (Bernauer and Brocks 2002). This phenomenological procedure can be used without the need for any extensive laboratory tests other than the standard tension coupon test.

Since fracture of structural steel could be by either the shear or the tensile mode, or a combination of both, it is important to employ models that are capable of capturing the two modes (Björklund et al 2013). To the best of the authors' knowledge, the prediction of tensile responses of civil engineering structural steel using the phenomenological shear fracture model

66 that simulates ductile tensile fracture under high stress triaxiality and employs the shear stress
67 ratio rather than the Lode angle parameter to simulate ductile shear fracture under low/negative
68 triaxiality has not been published. All the published fracture models on structural steel that
69 predict both ductile tensile fracture and ductile shear fracture employ the Lode angle parameter
70 for ductile shear fracture prediction.

71 The phenomenological shear damage and fracture model (Hooputra et al. 2004) presented in this
72 technical note simulates the ductile tensile fracture and the ductile shear fracture involving void
73 nucleation, void shearing and elongation, inter-voids shear localisation and void coalescence
74 under intense shear stresses (low and negative stress triaxiality). It is employed in the present
75 work to obtain the calibrated model parameters for S690 steel. The simulations of fractures of
76 TRIP (Transformation Induced Plasticity) 690 steel specimens under pure shear and under
77 combined shear and tension are also presented.

78 **Phenomenological shear damage and fracture model/criterion**

79 The phenomenological shear damage and fracture model employs the equivalent plastic strain as
80 the failure parameter (Hooputra et al. 2004). Shear damage initiation begins when the shear
81 damage initiation criterion, which is a function of the equivalent plastic strain ε_{eq}, is satisfied, as
82 shown in the following equation

83 $$\int_0^{\varepsilon_{eq}^{**}} \frac{d\varepsilon_{eq}}{\varepsilon_{eq}^{**}(\eta)} = 1 \qquad (1)$$

84 Equation (1) is satisfied when the equivalent plastic strain reaches the critical value ε_{eq}^{**} given by
85 Equation (2).

$$\varepsilon_{eq}^{**} = \frac{\varepsilon_S^+ \sinh\left[f(\theta_s^+ - \theta_s^-)\right] + \varepsilon_S^- \sinh\left[f(\theta_s^+ - \theta_s^-)\right]}{\sinh\left[f(\theta_s^+ - \theta_s^-)\right]} \quad (2)$$

$$\theta_s = \frac{(1 - k_s\eta)\sigma_{eq}}{\tau_{\max}} \quad (3)$$

The parameters ε_S^+ and ε_S^- are the equivalent plastic strains at shear damage initiation for equibiaxial tensile and compressive deformations, respectively, while f is an orientation dependent parameter and k_s is a material parameter. The first three parameters, which depend on the material type and the strain rate, "must" be determined experimentally. The variable η is the stress triaxiality. θ_s^+ and θ_s^- are the shear stress ratios for equibiaxial tension (at $\eta = \eta^+$) and compression (at $\eta = \eta^-$), respectively, which depend on the maximum shear stress $\tau_{\max}$, the equivalent stress σ_{eq} and the stress triaxility η, as shown in equation 3.

Shear damage initiation is associated with the progressive degradation of the elasticity or material stiffness which commences at the moment of the strain softening of the material at the point of the ultimate strength/stress (Henning 2012). Shear damage initiation is followed by damage evolution that is specified in terms of the equivalent plastic displacement, U^{pl}. Material failure typified by the complete loss of load-carrying capacity takes place in elements with completely degraded stiffness, which occurs when the equivalent plastic displacement U^{pl} reaches the critical value, the equivalent plastic displacement at failure U_f^{pl}. The equivalent plastic displacement at failure U_f^{pl} is specified as zero for instantaneous failure, and greater than zero (up to unity) for progressive failure. When the material fails, the damage variable d reaches its maximum value $d_{\max}$, and elements with completely degraded stiffness are either retained or

105 removed from the mesh. The default value of d_{max} is 1.0, but can be specified by the user as 0.99
106 (ABAQUS 2014).

107 **Calibration of S690 structural steel model parameters using phenomenological curve fitting**

108 Moze et al. (2007) conducted the tension coupon tests on S690 solid and perforated structural
109 steel coupons, depicted in Figures 1(a) and 1(b), respectively. The hole in the perforated tension
110 coupon H04 had a diameter of 10 mm, which was the same as the coupon thickness. The
111 elongation of each coupon was measured by Moze et al. (2007) over a gauge length of 280 mm.

112 The coupon models in Figures 1(c) and 1(d) were meshed with 1mm x 1mm x 1mm C3D8R
113 element that had been established through mesh convergence studies to be the appropriate
114 element size. C3D8R elements are 8-node hexahedral linear brick reduced integration elements
115 with hourglass control. Non-linear quasi-static analyses were conducted using the explicit solver
116 (ABAQUS 2014) at the default step time of one second to ensure that the kinetic energy is far
117 less than 5% of the total energy. The true stress-strain curves were calculated from the published
118 experimental force-displacement (Moze et al. 2007). The elastic modulus is assumed to be 200
119 GPa, with a Poisson's ratio of 0.3. The inelastic responses of the coupons were modelled with
120 the isotropic hardening rule and the von Mises yield criterion.

121 The experimental displacement at fracture of the solid coupon was not provided by Moze et al
122 (2007), so the calibration was conducted on the perforated coupon H04 instead, of which the
123 experimental displacement at fracture was 6.6 mm. The ultimate test load was 811 kN.

124 The phenomenological curve fitting process was conducted on the perforated coupon model with
125 the material parameter k_s and the equivalent plastic displacement at failure U_f^{pl} being kept

126 constant at 0.1 (Hooputra et al. 2004), while the equivalent plastic strain at shear fracture, shear
127 stress ratio and strain rate were varied, as shown in Table 1. Parameter combination A was the
128 experimentally calibrated values employed by Hooputra et al. (2004) for the simulation of ductile
129 fracture in aluminum alloy EN-AW-7108 TC. Parameter combinations B to E are linear
130 multiples (2.5, 3.0, 3.5, and 4.0) of the parameter combination A.

131 As shown in Table 2, parameter combination D resulted in the closest estimate of the
132 experimental displacement at fracture obtained by Moze et al (2007) for the perforated specimen
133 H04. The experimental load-displacement curve can be compared to that obtained using
134 parameter combination D in Figure 2.

135 In order to verify that the material parameter k_s has little if any significance in the S690 steel
136 tensile responses predicted using the phenomenological fracture model , eleven simulations were
137 conducted for the specimen H04 using the same parameters as the parameter combination D
138 except for the material parameter, which was varied from 0 to 10 at a step of 1. It was found that
139 all eleven simulations returned the same results as the parameter combination D, which had a
140 material parameter k_s equal to 0.1.

141 **FE predictions of the ultimate loads and displacements at fracture of perforated coupons**

142 In addition to the solid and perforated coupons H04 discussed in the preceding section, Moze et
143 al. (2007) tested perforated tension coupons with hole diameters of 5 mm, 13 mm, 18 mm, 22
144 mm, 26 mm, 30 mm, 40 mm and 50 mm, designated as specimens H03, H06, H07, H08, H10,
145 H12, H15 and H16, respectively. The load-displacement curves up to the displacement at
146 fracture predicted using the parameter combination D are shown in Figure 3. The ultimate loads
147 and displacements at fracture obtained numerically by the authors and experimentally by Moze

et al. (2007) are shown in Table 3. The variable R_{EP} represents the ratio of the experimental values to the predicted values.

Both the experimental tests (Moze et al. 2007) and the present simulations found that the perforated coupon with a 5-mm hole, H03, exhibited the largest displacements at fracture, being 9.0 mm and 10.7 mm, respectively. Incidentally, the difference between the experimental and the simulation results is the greatest for this coupon. In any case, the consistently accurate predictions of the tensile responses of the solid and perforated coupons, as evident in Table 3, demonstrate that the phenomenological shear damage and fracture model presented in this technical note is feasible and reliable.

Simulations of ductile fracture under pure shear and under combined shear and tension

In order to establish the ability of the present phenomenological shear damage and fracture model to predict fractures under pure shear and under combined shear and tension, the pure shear and the combined shear and tension loading tests of TRIP 690 steel specimens by Bai and Wierzbicki (2010) were simulated. The fracture simulation were conducted using a true yield stress of 445 MPa, a true tensile strength of 920MPa, a true yield strain of 0.02 and a true ultimate strain of 0.26 reported Li et al. (2010). An equivalent fracture strain of 1.1044, a shear stress ratio of 40, a strain rate of 0.00040 s^{-1}, a material parameter of 0.1 and an equivalent plastic displacement at failure of 0.1 were obtained through the phenomenological curve fitting process.

The models of the pure shear specimen and of the combined shear and tension specimen are shown in Figures 4(a) and 4(b), respectively. The gauge sections of both specimens were meshed

with 1mm x0.25mmx 0.25mm elements while the other sections were meshed with 1-mm cube elements. The loading pins were modeled as 3D analytical rigid cylindrical shells with the reference points at their base centers. The general contact (explicit) algorithm with the tangential behaviour penalty frictional interaction and a friction coefficient of 0.15 were employed to model the contact between the loading pins and the specimens. The top pins were fixed and the bottom pins were subjected to vertical downward displacements until the specimens fractured.

The predicted fracture processes of the specimens are shown in Figures 5 and 6 respectively. The failure of the specimen subjected to pure shear began with the initiation of a vertical fracture approximately parallel to the loading direction at the middle of the bottom end of the butterfly gauge section (Figure 5(a)), where the shear damage initiation criterion designated as SHRCRT (ABAQUS 2014) first reached its critical value of 1. The vertical fracture propagated upwards and the model fractured completely as shown in Figure 5(b). The failure of the specimen subjected to combined shear and tension began with the initiation of a fracture inclined to the loading direction at the top end of the strip gauge section, as shown in Figure 6(a). The initiated slanted fracture propagated downwards and the model fractured completely as shown in Figure 6(b).

Bao and Wierzbicki, (2004, 2010) were unable to capture the exact location of the fracture initiation and the fracture propagation. Consequently, the predicted fracture processes of the specimens subjected to pure shear and to combined shear and tension could not be validated against their experimental results. However, it can be seen from the good agreements between the experimental fracture shapes (Bao and Wierzbicki, 2010) and the simulated ones shown in Figure 7 that the present phenomenological shear damage and fracture model is capable of modelling fractures under pure shear and under combined shear and tension.

Conclusions

The predictions of structural steel tensile responses and fractures under tension, pure shear and combined shear and tension using the phenomenological shear fracture model that simulates ductile shear fracture based on the shear stress ratio (rather than the Lode angle parameter) has been presented. This technical note has covered the predictions of tensile responses of S690 steel solid coupons and perforated coupons having different hole diameters. It has also simulated the fractures of TRIP 690 steel specimens under pure shear and under combined shear and tension. The calibrated phenomenological shear damage and fracture model parameters, being the equivalent fracture strain, the shear stress ratio, the strain rate, the equivalent displacement at fracture and the material parameter were obtained through phenomenological curve fitting process. It has been found that the material parameter k_s has no noticeable effect on the shear damage and fracture, and the tensile responses (ultimate load and displacement at fracture) of structural steels

This technical note has demonstrated that the phenomenological shear fracture model can be employed in the design office for the predictions of ultimate loads and displacements at fracture required for the design of resilient or fracture-resistant steel structures, and for simulating the complete fracture process in structural steel. The phenomenological shear damage and fracture model parameters can be obtained through phenomenological curve fitting process that does not require costly laboratory tests.

213 Table 1. Parameter combinations for S690 steel

Parameter Combinations	Equivalent Fracture Strain ε_{eq}^{**}	Shear Stress Ratio θ_s^+	Strain Rate (s^{-1})	Material Parameter k_s	Equivalent Plastic Displacement at Failure
A	0.27610	10	0.00010	0.1	0.1
B	0.69025	25	0.00025	0.1	0.1
C	0.82830	30	0.00030	0.1	0.1
D	0.96635	35	0.00035	0.1	0.1
E	1.10440	40	0.00040	0.1	0.1

214

215 Table 2. Ultimate loads and displacements at fracture of perforated specimen H04

Parameter Combinations	Predicted Load (kN)	Difference (%)	Predicted Displacement at Fracture (mm)	Difference (%)
A	800	1.28	2.97	55.0
B	800	1.28	5.17	21.7
C	800	1.28	5.87	11.1
D	800	1.28	6.59	0.04
E	800	1.28	7.36	11.5

216

217 Table 3. Experimental and FE ultimate loads and displacements at fracture

Specimen	Hole Size (mm)	Ultimate Loads			Displacement at Fracture		
		Test (kN)	FE (kN)	R_{EP}	Test (mm)	FE (mm)	R_{EP}
H01	0	886	875	1.01	22.5	21.5	1.05
H03	5	861	860	1.00	9.0	10.7	0.84
H04	10	811	799	1.01	6.6	6.5	1.02
H06	13	789	782	1.01	7.0	6.9	1.01
H07	18	747	733	1.02	7.1	6.9	1.03
H08	22	716	702	1.02	7.1	7.3	0.97
H10	26	679	665	1.02	7.9	7.9	1.00
H12	30	641	627	1.02	8.0	7.9	1.01
H15	40	542	542	0.99	8.2	7.8	1.05
H16	50	456	454	1.00	8.4	9.2	0.91

218

219

References:

ABAQUS (2014) ABAQUS Analysis User's Manual, Version 6.14, Dassault Systèmes, Providence RI.

Bao, Y. and Wierzbicki, T. (2004) "On fracture locus in the equivalent strain and stress triaxiality space." *Int. J. Mech. Sci.*,46 , 81–98

Bai, Y. and Wierzbicki, T. (2008) "A new model of metal plasticity and fracture with pressure and Lode dependence." *Int. J. Plasticity,* 24, 1071–1096.

Bai, Y., Wierzbicki, T. (2010). "Application of extended Mohr–Coulomb criterion to ductile fracture."Int J Fract,161:1–20

Bernauer, G. and Brocks, W. (2002) "Micro-mechanical modelling of ductile damage and tearing–results of a European numerical round robin". *Fatigue and Frac. of Eng. Mat. & Struct.* , 25(4), 363-384.

Björklund, O., Larsson, R. and Nilsson, L. (2013) "Failure of high strength steel sheets: Experiments and modeling." *J. Mat. Proc. Tech.*, 213, 1103–1117.

Björklund, O. and Nilsson, L. (2014) "Failure characteristics of a dual-phase steel sheet." *J. Mat. Proc. Tech.*, 214, 1190–1204.

Cheng, L., Monchiet, V., Morin, L., Saxcé, G. and Kondo, D. (2015) "An analytical Lode angle dependent damage model for ductile porous materials." *Eng. Fract. Mech.*, 149, 119–133.

Danas, K. and Castañed, P. P. (2012) "Influence of the Lode parameter and the stress triaxiality on the failure of elasto-plastic porous materials." *Int. J. Solids and Struct.*, 49, 1325–1342.

French, I. E. and Weinrich, P. F. (1979) "The shear mode of ductile failure in mild steel." *Mat. Sci. Eng.*, 39 (1), 43-46.

242 Gologanu, M., Leblond, J. B. and Devaux, J. (1993) "Approximate models for ductile metals
243 containing nonspherical voids – case of axisymmetrical prolate ellipsoidal cavities". *J. Mech.*
244 *Phys. Solids*, 41 (11), 1723–1754.
245 Henning, L. (2012). *Simulating Ductile Fracture in Steel using the Finite Element Method:*
246 *Comparison of Two Models For Describing Local Instability due to Ductile Fracture*, MSc
247 thesis, Faculty of Mathematics and Natural Sciences, University of Oslo, Norway.
248 Hooputra, H., Gese, H., Dell, H., and Werner, H. A. (2004) "Comprehensive failure model for
249 crashworthiness simulation of aluminium extrusions." *Int. J. Crashworthiness*, 9 (5), 449–64.
250 Jia, L. and Kuwamura, H. (2014) "Ductile Fracture Simulation of Structural Steels under
251 Monotonic Tension." *J. Struct. Eng.*, DOI: 10.1061/(ASCE)ST.1943-541X.0000944
252 Kanvinde, A. M. and Deierlein, G. G. (2006) **"**The Void Growth Model and the Stress Modified
253 Critical Strain Model to Predict Ductile Fracture in Structural Steels." *J. Struct. Eng.*,
254 10.1061/(ASCE)0733-9445(2006)132:12(1907).
255 Kiran, R., and Khandelwal, K. (2013) "A micromechanical model for ductile fracture prediction
256 in ASTM A992 steels." *Eng. Frac. Mech.*, 102, 101-117.
257 Li, W., Liao, F. Zhou, T., and Askes, H. (2016) "Ductile fracture of Q460 steel: Effects of stress
258 triaxiality and Lode angle." *J. Construct. Steel Res.*, 123, 1–17.
259 Li, Y., Luo M., Gerlach, J., and Wierzbicki, T. (2010) "Prediction of shear-induced fracture in
260 sheet metal forming." *J. Mat. Proc. Tech.*, 210, 1858–1869.
261 Moze, P., Beg, D. and Lopati, J. (2007) "Net cross-section design resistance and local ductility of
262 elements made of high strength steel." *J. Construct. Steel Res.*, 63, 1431–1441.
263 Nahshon, K. and Hutchinson, J. W. (2008) "Modification of the Gurson model for shear
264 fracture." *Euro. J. Mech. Solids*, 27, 1–17.

265 Rice, J. R. and Tracey, D. M. (1969) "On the ductile enlargement of voids in triaxial stress
266 fields." *J. Mech. Phys. Solids*, 17, 201-217.
267 Wen, H. and Mahmoud, H. (2015) "New Model for Ductile Fracture of Metal Alloys. I:
268 Monotonic Loading." *J. Eng. Mech.*, DOI: 10.1061/(ASCE) EM.1943-7889.0001009.
269 Wilkins, M. L., Streit, R. D. and Reaugh, J. E. (1980) "Cumulative strain- damage model of
270 ductile fracture: simulation and prediction of engineering fracture tests." *Research Report*
271 *No. UCRL-53058*, Science Applications, San Leandro, CA.
272 Xue, L. (2008) "Constitutive modeling of void shearing effect in ductile fracture of porous
273 materials." *Eng. Frac. Mech.*, 75, 3343–3366.

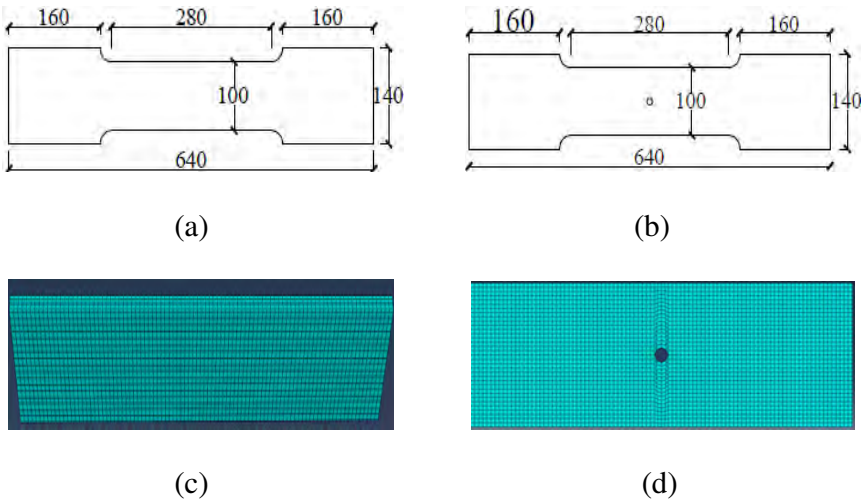

Figure 1 Test specimens and FE models: (a) Solid tension coupon (H01); (b) Perforated coupon (H04); (c) Solid coupon's FE model; (d) Perforated coupon's FE model.

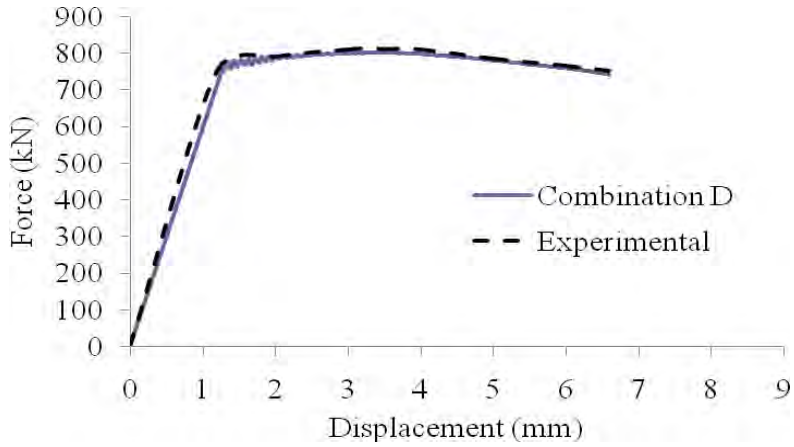

Figure 2 Experimental and analysis results of H04 using parameter combination D

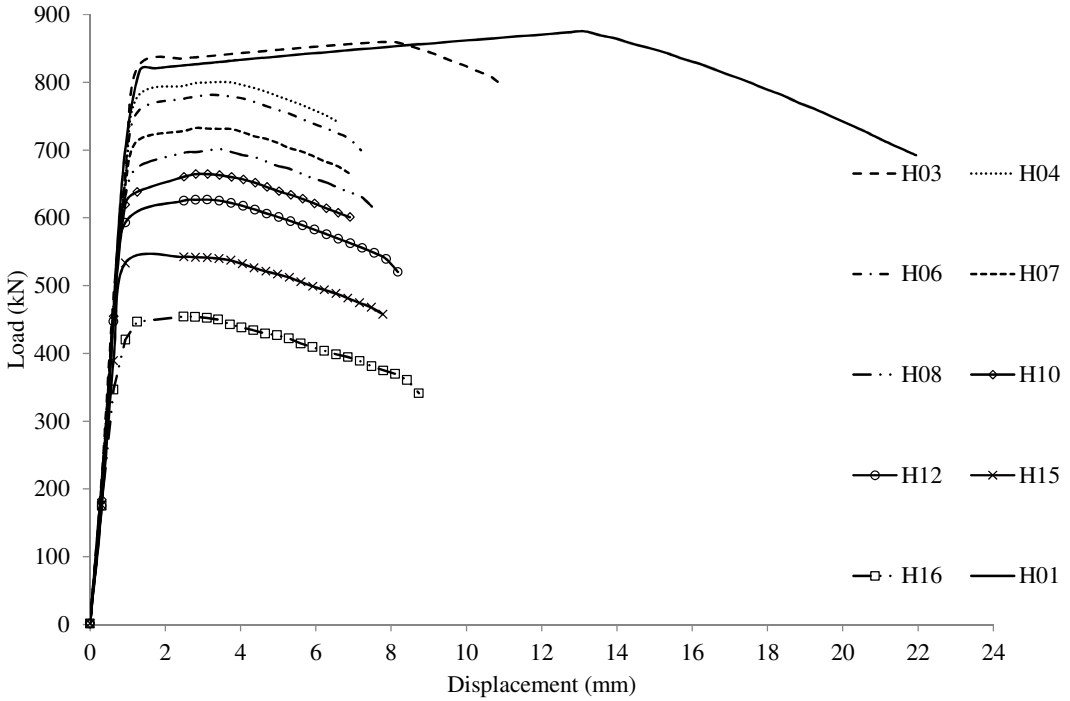

Figure 3 Force-displacement curves for solid coupon (H01) and perforated coupons with varying hole diameters using parameter combination D

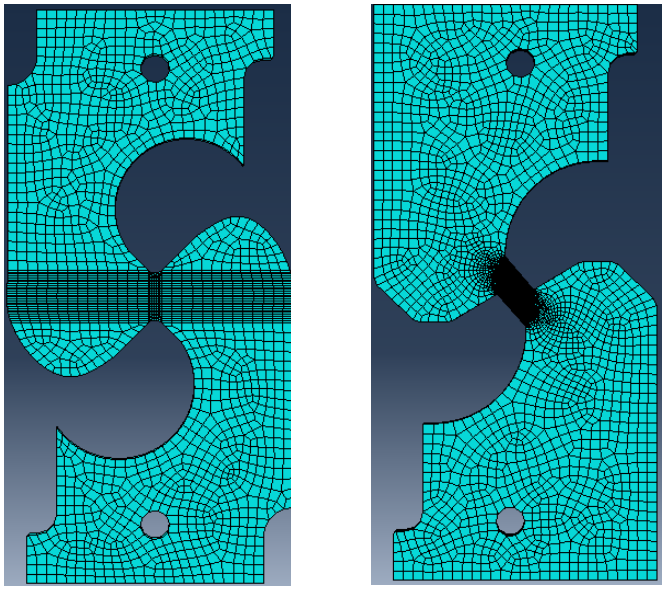

(a) (b)

Figure 4: FE models of: (a) Pure shear specimen; (b) Combined shear and tension specimen

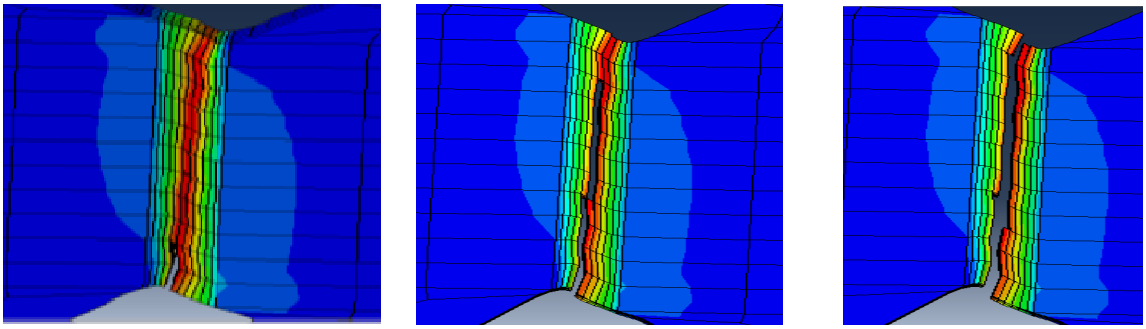

(a) (b) (c)

Figure 5: Predicted fracture processes of the specimen subjected to pure shear: (a) Fracture initiation; (b) Fracture propagation; (c) Complete fracture

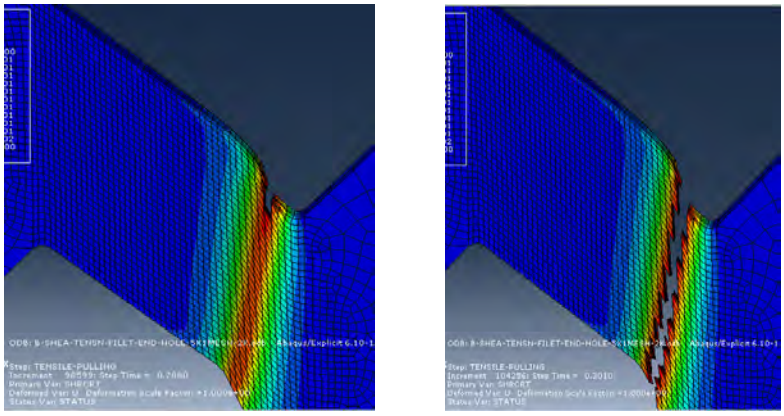

Figure 6: Predicted fracture processes of the specimen subjected to combined shear and tension: (a) Fracture initiation and propagation; (b) Complete fracture

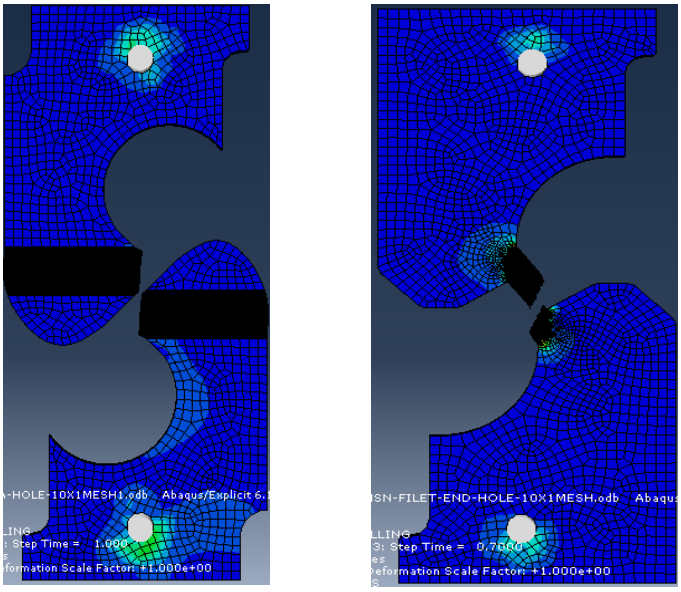

(a) (b)

Figure 7: Predicted fractured shapes: (a) Pure shear specimen; (b) Combined shear and tension specimen